Measurements of the time-dependent cosmic-ray Sun shadow with seven years of IceCube data: Comparison with the Solar cycle and magnetic field models

M. G. Aartsen,[17] R. Abbasi,[16] M. Ackermann,[56] J. Adams,[17] J. A. Aguilar,[12] M. Ahlers,[21] M. Ahrens,[47] C. Alispach,[27] N. M. Amin,[40] K. Andeen,[38] T. Anderson,[53] I. Ansseau,[12] G. Anton,[25] C. Argüelles,[14] J. Auffenberg,[1] S. Axani,[14] H. Bagherpour,[17] X. Bai,[44] A. V. Balagopal,[30] A. Barbano,[27] S. W. Barwick,[29] B. Bastian,[56] V. Basu,[36] V. Baum,[37] S. Baur,[12] R. Bay,[8] J. J. Beatty,[19,20] K.-H. Becker,[55] J. Becker Tjus,[11] S. BenZvi,[46] D. Berley,[18] E. Bernardini,[56,*] D. Z. Besson,[31,†] G. Binder,[8,9] D. Bindig,[55] E. Blaufuss,[18] S. Blot,[56] C. Bohm,[57] S. Böser,[37] O. Botner,[54] J. Böttcher,[1] E. Bourbeau,[21] J. Bourbeau,[36] F. Bradascio,[56] J. Braun,[36] S. Bron,[27] J. Brostean-Kaiser,[56] A. Burgman,[54] J. Buscher,[1] R. S. Busse,[39] T. Carver,[27] C. Chen,[6] E. Cheung,[18] D. Chirkin,[36] S. Choi,[49] B. A. Clark,[23] K. Clark,[32] L. Classen,[39] A. Coleman,[58] G. H. Collin,[14] J. M. Conrad,[14] P. Coppin,[13] P. Correa,[13] D. F. Cowen,[52,53] R. Cross,[46] P. Dave,[6] C. De Clercq,[13] J. J. DeLaunay,[53] H. Dembinski,[58] K. Deoskar,[57] S. De Ridder,[28] A. Desai,[36] P. Desiati,[36] K. D. de Vries,[13] G. de Wasseige,[13] M. de With,[10] T. DeYoung,[23] S. Dharani,[1] A. Diaz,[14] J. C. Díaz-Vélez,[36] H. Dujmovic,[30] M. Dunkman,[53] M. A. DuVernois,[36] E. Dvorak,[44] T. Ehrhardt,[37] P. Eller,[53] R. Engel,[30] P. A. Evenson,[58] S. Fahey,[36] A. R. Fazely,[7] J. Felde,[18] H. Fichtner,[11] A. T. Fienberg,[53] K. Filimonov,[8] C. Finley,[57] D. Fox,[52] A. Franckowiak,[56] E. Friedman,[18] A. Fritz,[37] T. K. Gaisser,[58] J. Gallagher,[35] E. Ganster,[1] S. Garrappa,[56] L. Gerhardt,[9] A. Ghadimi,[51] T. Glauch,[26] T. Glüsenkamp,[25] A. Goldschmidt,[9] J. G. Gonzalez,[58] S. Goswami,[51] D. Grant,[23] T. Grégoire,[53] Z. Griffith,[36] S. Griswold,[46] M. Günder,[1] M. Gündüz,[11] C. Haack,[1] A. Hallgren,[54] R. Halliday,[23] L. Halve,[1] F. Halzen,[36] K. Hanson,[36] J. Hardin,[36] A. Haungs,[30] S. Hauser,[1] D. Hebecker,[10] D. Heereman,[12] P. Heix,[1] K. Helbing,[55] R. Hellauer,[18] F. Henningsen,[26] S. Hickford,[55] J. Hignight,[24] C. Hill,[15] G. C. Hill,[2] K. D. Hoffman,[18] R. Hoffmann,[55] T. Hoinka,[22] B. Hokanson-Fasig,[36] K. Hoshina,[36,‡] F. Huang,[53] M. Huber,[26] T. Huber,[30,56] K. Hultqvist,[57] M. Hünnefeld,[22] R. Hussain,[36] S. In,[49] N. Iovine,[12] A. Ishihara,[15] M. Jansson,[57] G. S. Japaridze,[5] M. Jeong,[49] B. J. P. Jones,[4] F. Jonske,[1] R. Joppe,[1] D. Kang,[30] W. Kang,[49] A. Kappes,[39] D. Kappesser,[37] T. Karg,[56] M. Karl,[26] A. Karle,[36] U. Katz,[25] M. Kauer,[36] M. Kellermann,[1] J. L. Kelley,[36] A. Kheirandish,[53] J. Kim,[49] K. Kin,[15] T. Kintscher,[56] J. Kiryluk,[48] T. Kittler,[25] J. Kleimann,[11] S. R. Klein,[8,9] R. Koirala,[58] H. Kolanoski,[10] L. Köpke,[37] C. Kopper,[23] S. Kopper,[51] D. J. Koskinen,[21] P. Koundal,[30] M. Kowalski,[10,56] K. Krings,[26] G. Krückl,[37] N. Kulacz,[24] N. Kurahashi,[43] A. Kyriacou,[2] J. L. Lanfranchi,[53] M. J. Larson,[18] F. Lauber,[55] J. P. Lazar,[36] K. Leonard,[36] A. Leszczyńska,[30] Y. Li,[53] Q. R. Liu,[36] E. Lohfink,[37] C. J. Lozano Mariscal,[39] L. Lu,[15] F. Lucarelli,[27] A. Ludwig,[33] J. Lünemann,[13] W. Luszczak,[36] Y. Lyu,[8,9] W. Y. Ma,[56] J. Madsen,[45] G. Maggi,[13] K. B. M. Mahn,[23] Y. Makino,[36] P. Mallik,[1] S. Mancina,[36] I. C. Mariş,[12] R. Maruyama,[41] K. Mase,[15] R. Maunu,[18] F. McNally,[34] K. Meagher,[36] M. Medici,[21] A. Medina,[20] M. Meier,[15] S. Meighen-Berger,[26] J. Merz,[1] T. Meures,[12] J. Micallef,[23] D. Mockler,[12] G. Momenté,[37] T. Montaruli,[27] R. W. Moore,[24] R. Morse,[36] M. Moulai,[14] P. Muth,[1] R. Nagai,[15] U. Naumann,[55] G. Neer,[23] L. V. Nguyễn,[23] H. Niederhausen,[26] M. U. Nisa,[23] S. C. Nowicki,[23] D. R. Nygren,[9] A. Obertacke Pollmann,[55] M. Oehler,[30] A. Olivas,[18] A. O'Murchadha,[12] E. O'Sullivan,[54] H. Pandya,[58] D. V. Pankova,[53] N. Park,[36] G. K. Parker,[4] E. N. Paudel,[58] P. Peiffer,[37] C. Pérez de los Heros,[54] S. Philippen,[1] D. Pieloth,[22] S. Pieper,[55] E. Pinat,[12] A. Pizzuto,[36] M. Plum,[38] Y. Popovych,[1] A. Porcelli,[28] M. Prado Rodriguez,[36] P. B. Price,[8] G. T. Przybylski,[9] C. Raab,[12] A. Raissi,[17] M. Rameez,[21] L. Rauch,[56] K. Rawlins,[3] I. C. Rea,[26] A. Rehman,[58] R. Reimann,[1] B. Relethford,[43] M. Renschler,[30] G. Renzi,[12] E. Resconi,[26] W. Rhode,[22] M. Richman,[43] B. Riedel,[36] S. Robertson,[8,9] G. Roellinghoff,[49] M. Rongen,[1] C. Rott,[49] T. Ruhe,[22] D. Ryckbosch,[28] D. Rysewyk Cantu,[23] I. Safa,[36] S. E. Sanchez Herrera,[23] A. Sandrock,[22] J. Sandroos,[37] M. Santander,[51] S. Sarkar,[42] S. Sarkar,[24] K. Satalecka,[56] M. Scharf,[1] M. Schaufel,[1] H. Schieler,[30] P. Schlunder,[22] T. Schmidt,[18] A. Schneider,[36] J. Schneider,[25] F. G. Schröder,[30,58] L. Schumacher,[1] S. Sclafani,[43] D. Seckel,[58] S. Seunarine,[45] S. Shefali,[1] M. Silva,[36] B. Smithers,[4] R. Snihur,[36] J. Soedingrekso,[22] D. Soldin,[58] M. Song,[18] G. M. Spiczak,[45] C. Spiering,[56] J. Stachurska,[56] M. Stamatikos,[20] T. Stanev,[58] R. Stein,[56] J. Stettner,[1] A. Steuer,[37] T. Stezelberger,[9] R. G. Stokstad,[9] N. L. Strotjohann,[56] T. Stürwald,[1] T. Stuttard,[21] G. W. Sullivan,[18] I. Taboada,[6] F. Tenholt,[11] S. Ter-Antonyan,[7] A. Terliuk,[56] S. Tilav,[58] K. Tollefson,[23] L. Tomankova,[11] C. Tönnis,[50] S. Toscano,[12] D. Tosi,[36] A. Trettin,[56] M. Tselengidou,[25] C. F. Tung,[6] A. Turcati,[26] R. Turcotte,[30] C. F. Turley,[53] B. Ty,[36] E. Unger,[54] M. A. Unland Elorrieta,[39] M. Usner,[56] J. Vandenbroucke,[36] W. Van Driessche,[28] D. van Eijk,[36] N. van Eijndhoven,[13] D. Vannerom,[14] J. van Santen,[56] S. Verpoest,[28] M. Vraeghe,[28] C. Walck,[57] A. Wallace,[2] M. Wallraff,[1] T. B. Watson,[4] C. Weaver,[24] A. Weindl,[30] M. J. Weiss,[53] J. Weldert,[37] C. Wendt,[36] J. Werthebach,[22] B. J. Whelan,[2] N. Whitehorn,[33] K. Wiebe,[37] C. H. Wiebusch,[1] D. R. Williams,[51] L. Wills,[43] M. Wolf,[26] T. R. Wood,[24] K. Woschnagg,[8] G. Wrede,[25] J. Wulff,[11] X. W. Xu,[7] Y. Xu,[48] J. P. Yanez,[24] S. Yoshida,[15] T. Yuan,[36] Z. Zhang,[48] and M. Zöcklein[1]

(IceCube Collaboration)

[1]*III. Physikalisches Institut, RWTH Aachen University, D-52056 Aachen, Germany*
[2]*Department of Physics, University of Adelaide, Adelaide, 5005, Australia*
[3]*Department of Physics and Astronomy, University of Alaska Anchorage, 3211 Providence Dr., Anchorage, Alaska 99508, USA*
[4]*Department of Physics, University of Texas at Arlington, 502 Yates St., Science Hall Rm 108, Box 19059, Arlington, Texas 76019, USA*
[5]*CTSPS, Clark-Atlanta University, Atlanta, Georgia 30314, USA*
[6]*School of Physics and Center for Relativistic Astrophysics, Georgia Institute of Technology, Atlanta, Georgia 30332, USA*
[7]*Department of Physics, Southern University, Baton Rouge, Louisiana 70813, USA*
[8]*Department of Physics, University of California, Berkeley, California 94720, USA*
[9]*Lawrence Berkeley National Laboratory, Berkeley, California 94720, USA*
[10]*Institut für Physik, Humboldt-Universität zu Berlin, D-12489 Berlin, Germany*
[11]*Fakultät für Physik & Astronomie, Ruhr-Universität Bochum, D-44780 Bochum, Germany*
[12]*Université Libre de Bruxelles, Science Faculty CP230, B-1050 Brussels, Belgium*
[13]*Vrije Universiteit Brussel (VUB), Dienst ELEM, B-1050 Brussels, Belgium*
[14]*Department of Physics, Massachusetts Institute of Technology, Cambridge, Massachusetts 02139, USA*
[15]*Department of Physics and Institute for Global Prominent Research, Chiba University, Chiba 263-8522, Japan*
[16]*Department of Physics, Loyola University Chicago, Chicago, Illinois 60660, USA*
[17]*Department of Physics and Astronomy, University of Canterbury, Private Bag 4800, Christchurch, New Zealand*
[18]*Department of Physics, University of Maryland, College Park, Maryland 20742, USA*
[19]*Department of Astronomy, Ohio State University, Columbus, Ohio 43210, USA*
[20]*Department of Physics and Center for Cosmology and Astro-Particle Physics, Ohio State University, Columbus, Ohio 43210, USA*
[21]*Niels Bohr Institute, University of Copenhagen, DK-2100 Copenhagen, Denmark*
[22]*Department of Physics, TU Dortmund University, D-44221 Dortmund, Germany*
[23]*Department of Physics and Astronomy, Michigan State University, East Lansing, Michigan 48824, USA*
[24]*Department of Physics, University of Alberta, Edmonton, Alberta, Canada T6G 2E1*
[25]*Erlangen Centre for Astroparticle Physics, Friedrich-Alexander-Universität Erlangen-Nürnberg, D-91058 Erlangen, Germany*
[26]*Physik-department, Technische Universität München, D-85748 Garching, Germany*
[27]*Département de physique nucléaire et corpusculaire, Université de Genève, CH-1211 Genève, Switzerland*
[28]*Department of Physics and Astronomy, University of Gent, B-9000 Gent, Belgium*
[29]*Department of Physics and Astronomy, University of California, Irvine, California 92697, USA*
[30]*Karlsruhe Institute of Technology, Institut für Kernphysik, D-76021 Karlsruhe, Germany*
[31]*Department of Physics and Astronomy, University of Kansas, Lawrence, Kansas 66045, USA*
[32]*SNOLAB, 1039 Regional Road 24, Creighton Mine 9, Lively, ON, Canada P3Y 1N2*
[33]*Department of Physics and Astronomy, UCLA, Los Angeles, California 90095, USA*
[34]*Department of Physics, Mercer University, Macon, Georgia 31207-0001, USA*
[35]*Department of Astronomy, University of Wisconsin, Madison, Wisconsin 53706, USA*
[36]*Department of Physics and Wisconsin IceCube Particle Astrophysics Center, University of Wisconsin, Madison, Wisconsin 53706, USA*
[37]*Institute of Physics, University of Mainz, Staudinger Weg 7, D-55099 Mainz, Germany*
[38]*Department of Physics, Marquette University, Milwaukee, Wisconsin 53201, USA*
[39]*Institut für Kernphysik, Westfälische Wilhelms-Universität Münster, D-48149 Münster, Germany*
[40]*Bartol Research Institute and Dept. of Physics and Astronomy, University of Delaware, Newark, Delaware 19716, USA*
[41]*Department of Physics, Yale University, New Haven, Connecticut 06520, USA*
[42]*Department of Physics, University of Oxford, Parks Road, Oxford OX1 3PU, UK*
[43]*Department of Physics, Drexel University, 3141 Chestnut Street, Philadelphia, Pennsylvania 19104, USA*
[44]*Physics Department, South Dakota School of Mines and Technology, Rapid City, South Dakota SD 57701, USA*
[45]*Department of Physics, University of Wisconsin, River Falls, Wisconsin 54022, USA*
[46]*Department of Physics and Astronomy, University of Rochester, Rochester, New York 14627, USA*

[47]Oskar Klein Centre and Dept. of Physics, Stockholm University, SE-10691 Stockholm, Sweden
[48]Department of Physics and Astronomy, Stony Brook University, Stony Brook, New York 11794-3800, USA
[49]Department of Physics, Sungkyunkwan University, Suwon 16419, Korea
[50]Institute of Basic Science, Sungkyunkwan University, Suwon 16419, Korea
[51]Department of Physics and Astronomy, University of Alabama, Tuscaloosa, Alabama 35487, USA
[52]Department of Astronomy and Astrophysics, Pennsylvania State University, University Park, Pennsylvania 16802, USA
[53]Department of Physics, Pennsylvania State University, University Park, Pennsylvania 16802, USA
[54]Department of Physics and Astronomy, Uppsala University, Box 516, S-75120 Uppsala, Sweden
[55]Department of Physics, University of Wuppertal, D-42119 Wuppertal, Germany
[56]DESY, D-15738 Zeuthen, Germany
[57]Oskar Klein Centre and Department of Physics, Stockholm University, SE-10691 Stockholm, Sweden
[58]Bartol Research Institute and Department of Physics and Astronomy, University of Delaware, Newark, Delaware 19716, USA

(Received 26 June 2020; accepted 11 December 2020; published 8 February 2021)

Observations of the time-dependent cosmic-ray Sun shadow have been proven as a valuable diagnostic for the assessment of solar magnetic field models. In this paper, seven years of IceCube data are compared to solar activity and solar magnetic field models. A quantitative comparison of solar magnetic field models with IceCube data on the event rate level is performed for the first time. Additionally, a first energy-dependent analysis is presented and compared to recent predictions. We use seven years of IceCube data for the moon and the Sun and compare them to simulations on data rate level. The simulations are performed for the geometrical shadow hypothesis for the moon and the Sun and for a cosmic-ray propagation model governed by the solar magnetic field for the case of the Sun. We find that a linearly decreasing relationship between Sun shadow strength and solar activity is preferred over a constant relationship at the 6.4σ level. We test two commonly used models of the coronal magnetic field, both combined with a Parker spiral, by modeling cosmic-ray propagation in the solar magnetic field. Both models predict a weakening of the shadow in times of high solar activity as it is also visible in the data. We find tensions with the data on the order of 3σ for both models, assuming only statistical uncertainties. The magnetic field model CSSS fits the data slightly better than the PFSS model. This is generally consistent with what is found previously by the Tibet AS-γ Experiment; a deviation of the data from the two models is, however, not significant at this point. Regarding the energy dependence of the Sun shadow, we find indications that the shadowing effect increases with energy during times of high solar activity, in agreement with theoretical predictions.

DOI: 10.1103/PhysRevD.103.042005

I. INTRODUCTION

The existence of the cosmic-ray Sun shadow, which commonly refers to cosmic rays being blocked by the Sun, has first been suggested by George W. Clark in 1957 [1]. While cosmic rays that propagate close to the moon are only deflected marginally by the geomagnetic and heliospheric magnetic fields, cosmic rays that traverse the coronal solar magnetic field can be deflected strongly and irregularly.

Hence, the cosmic-ray moon shadow essentially blocks cosmic rays from a well-known solid angle and can be used as a direction and resolution standard. Several experiments have exploited this feature to study their angular resolution, absolute pointing, and absolute energy scale,[1] e.g., Tibet AS-γ, MILAGRO, MACRO, Soudan2, ARGO-YBJ, and IceCube [2–7].

The cosmic-ray Sun shadow, on the other hand, contains the footprint of the solar magnetic field in the form of those cosmic rays reaching Earth that come from directions close to the Sun. In 2013, the Tibet AS-γ Collaboration compared coronal magnetic field models using the cosmic-ray Sun shadow at a median primary cosmic-ray energy of ∼10 TeV [8]. Later, they also studied the influence of solar coronal mass ejections (CMEs) on the cosmic-ray Sun shadow at energies of ∼3 TeV [9] and concluded that Earth-directed CMEs (ECMEs) affect the cosmic-ray Sun shadow at these energies. The influence of the solar

*Also at Università di Padova, I-35131 Padova, Italy
†Also at National Research Nuclear University, Moscow Engineering Physics Institute (MEPhI), Moscow 115409, Russia
‡Earthquake Research Institute, University of Tokyo, Bunkyo, Tokyo 113-0032, Japan

[1]The latter is done by using the energy-dependent shift of the position of the shadow due to the Earth's magnetic field.

magnetic field on the cosmic-ray Sun shadow has been studied by several other experiments, like Milagro, ARGO-YBJ, and HAWC, as well [10–12]. Such efforts are especially important since no *in situ* measurements of the solar magnetic field closer than to about 0.29 ua (≈62 solar radii) distance from the Sun Helios spacecraft [13]) existed until very recently. Even the Parker Solar Probe, which will eventually approach the Sun up to ∼8.9 solar radii in 2024 [14], has as of yet not been closer than 27.8 solar radii, i.e., about 0.13 ua.

In this paper, we investigate a possible time dependence of the cosmic-ray Sun shadow using seven years of IceCube data. The measurements are based on atmospheric muons detected with IceCube, induced by cosmic rays entering the Earth's atmosphere. For the first time, we use IceCube data for a comparison of measurements with the expected shadow for solar activity with different solar magnetic field models. We calculate the median energy of the primary cosmic rays in our sample to 50–60 TeV, depending on the cosmic-ray flux model that is used to derive cosmic-ray energies from the measured muons. This is, therefore, the highest energy measurement of the Sun shadow so far, as compared to the median primary cosmic-ray energies of the earlier measurements that lie around 1–10 TeV. Additionally, the energy dependence of the Sun shadow is investigated; i.e., two samples with respective median energies of 40 TeV and 100 TeV are produced and qualitatively compared to a recent prediction, in which the energy-dependence of the Sun shadow in a low-activity solar magnetic field is shown to differ significantly from that in a high-activity solar magnetic field [15]. The data we use for studying the cosmic-ray Sun shadow in IceCube comprise the time from late 2010 until early 2017 and cover large parts of Solar Cycle 24. This cycle is defined for the time interval from late 2008 to some time around late 2019 to early 2020, wherein the exact location of the minimum that defines the end of the cycle is not clear at this point. This work follows an earlier study, which reported on the detection of a temporal variation of the cosmic-ray Sun shadow measured with IceCube and found a correlation with solar activity to be likely [16].

II. THE ICECUBE NEUTRINO OBSERVATORY

The IceCube Neutrino Observatory is a detection array deployed in the Antarctic ice near the geographic South Pole and comprises a volume of about 1 km^3 instrumented with 5160 digital optical modules (DOMs) on 86 strings [17]. IceCube is located at a depth between 1450 m and 2450 m and detects relativistic secondary particles induced

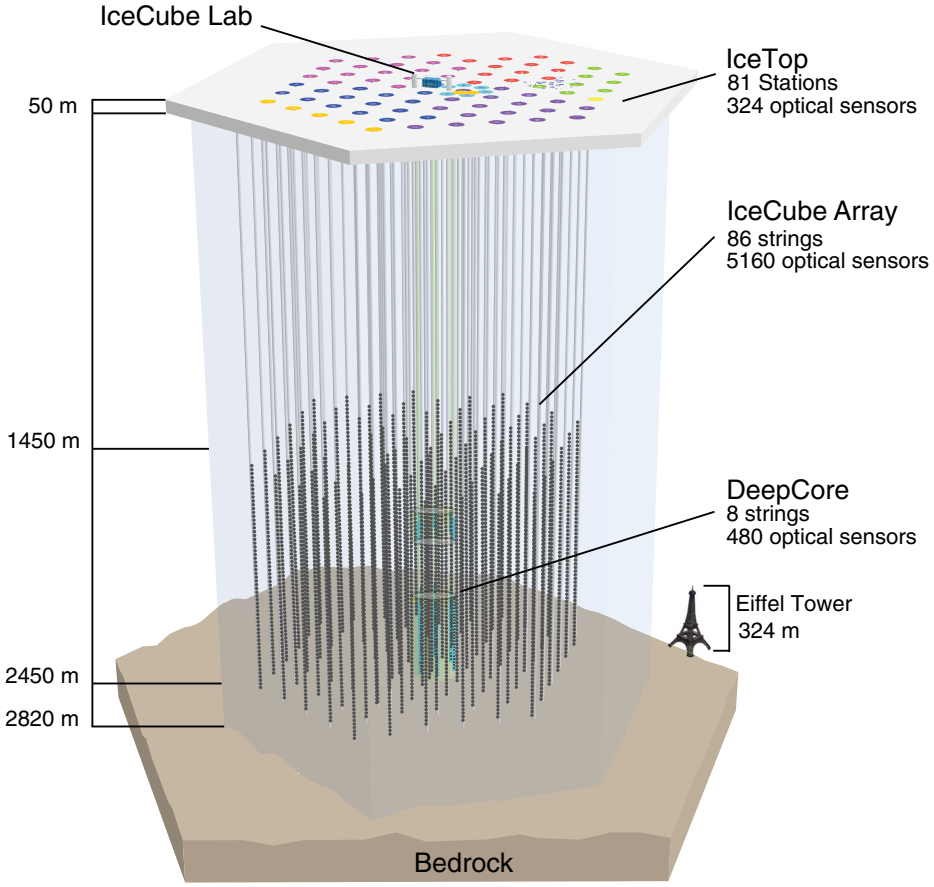

FIG. 1. The IceCube Neutrino Observatory.

by astrophysical neutrinos, gamma rays, and cosmic rays. The detector was built at the South Pole between 2005 and 2010 and exploits the clear Antarctic ice as its detection medium for Cherenkov radiation of charged particles traversing it.

A sketch of the IceCube Neutrino Observatory including its subarray DeepCore [18], which aims to improve the sensitivity to lower-energy neutrinos, can be seen in Figure 1. Data from DeepCore have not been used in this analysis. For neutrinos, IceCube's main array has an energy threshold of about 100 GeV. In this paper, we use atmospheric muons, which are a background to the neutrino searches. In this sample, the energies of the primary cosmic rays inducing these atmospheric muon events are typically $\gtrsim$1 TeV.

III. DATA SAMPLE

In IceCube, high-energy muons are observed. As these are predominantly produced by cosmic-ray air showers, they trace the direction of the primary particles, with the angular uncertainty being dominated by the uncertainty of the light propagation in the ice and limited by the kinematic angle between primary and secondary particle. We thus measure an event rate of high-energy muons in IceCube. The event rate increases with increasing elevation because of the decreasing amount of ice overburden that cosmic-ray induced atmospheric muons have to cross to reach the detector. In this section, we describe the details of our data sample.

A. Moon and Sun as seen from the South Pole

This paper uses data from IceCube's 79-string configuration (IC79), which was available in the 2010/2011 season and from the final 86-string configuration (IC86), which was available from the 2011/2012 season and onward. We use the high-energy atmospheric muons that pass through the detector for our analysis, as they are direct tracers of the primary particles. The strength of the cosmic-ray shadow of the moon and Sun is determined by the number of cosmic rays that are blocked. Without additional forces, this number results from the solid angle that is spanned by the moon and the Sun as seen from Earth, i.e., their angular radii. Using their respective physical radii R and distances d from Earth, the (apparent) angular radius R_{app} of the moon and Sun as seen from Earth is calculated as

$$R_{\mathrm{app}} = \arctan\left(R/d\right). \tag{1}$$

The values for R and d are taken from [[19], p. 447, Table C.6, p. 450, Table C.13] and [[19], pp. 134–135], respectively.

The resulting minimum and maximum angular radii of the moon and Sun as seen from the South Pole amount to 0.245° to 0.279° for the moon and 0.262° to 0.271° for the Sun.

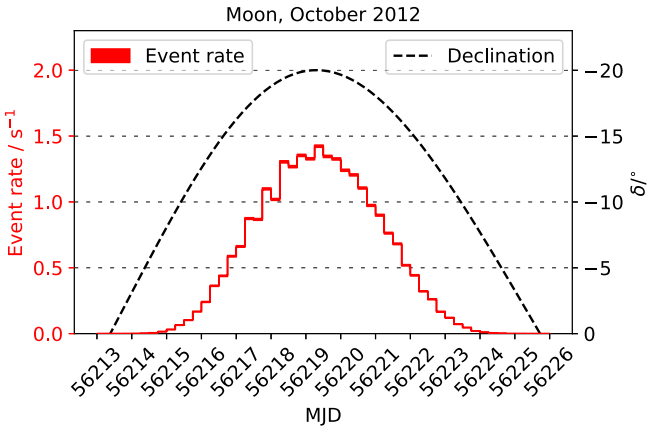

FIG. 2. Comparison of moon declination δ and final moon shadow sample event rate. At the South Pole, the elevation of an object equals $-\delta$.

Notably, both objects have an angular diameter of ∼0.5°, which makes a comparison relatively straightforward.

The maximum elevation of the moon at the South Pole varies between 18.3° and 28.6° due to its orbital inclination and Earth's axial tilt. While the Earth axial tilt changes only very slowly, the moon's orbital inclination varies with a nodal period of about 18.6 years. For the Sun's elevation, on the other hand, only the Earth axial tilt is relevant for its maximum elevation, which amounts to about 23.4° each year. The Sun rises and sets only once per year at the South Pole, resulting in one continuous observation period approximately from November through February each year. The moon instead rises and sets approximately every 27 days, which leads to about 13 separate observation periods. An example of one such period is shown in Figure 2. As can be seen in Figure 2, when the elevation of the moon (same for the Sun) is below ∼7.5°, the event rate drops essentially to zero. Therefore, the final moon and Sun shadow data samples (cf. next section) contain almost no events for such small elevations of moon and Sun. As a result, the background or signal regions of the final data sample are unaffected by possible boundary effects close to the horizon. Such effects are also prevented by choosing the background from the same zenith band as the Sun. Elevation and declination values given above and shown in Figure 2 have been calculated using ASTROPY [20,21] and its built-in ERFA routines [22].

B. Data selection and quality cuts

At the South Pole, the direction of each muon event is reconstructed using a comparably simple and thus fast maximum-likelihood method (cf. [23] for details). Since atmospheric muons detected in IceCube are ultrarelativistic, the opening angle between muon direction and primary cosmic-ray direction, which is on the order of 0.1° for multi-TeV muons [7], is part of the directional uncertainty

between the actual primary cosmic-ray direction and the reconstructed event direction. Data are only taken when the moon and Sun are above the horizon (at least 15° above the horizon for data between May 2010 and May 2012; as in these early years, directional reconstruction near the horizon was not good enough). These moon and Sun filters are implemented at the South Pole and are necessary in order to reduce the data to a manageable amount for satellite data transmission to the Northern hemisphere.

For further event reconstruction, a ±10° zenith band (±180° in azimuth) around the known position of moon and Sun in the sky is considered. While this full azimuth band is available at the low-level of the analysis, the six off-source regions that we chose only make use of parts of this band, in total 54° × 6°. The reason not to include more off-source regions is that it would increase the processing (and final data file sizes), while not substantially reducing the statistical uncertainty.

The events are then selected with the requirement to hit at least eight DOMs on three different strings.

After the first selection at the South Pole, the data are transferred North and more sophisticated reconstruction algorithms are applied to the following parameters: Besides the multi-photo-electron (MPE) fit [23], which accounts for the total number of Cherenkov photons collected by each DOM, this includes a paraboloid fit to the likelihood profile of the directional coordinates [24].

To ensure that only well-reconstructed events are used for the final data analysis, two quality cuts based on these reconstructions are applied:

(1) The reduced log-likelihood (rlogl), which represents the goodness of fit of the MPE reconstruction, is required to satisfy rlogl < 8.1, see [24].
(2) The angular uncertainty σ, which is derived from the paraboloid fit to the likelihood profile,[2] is required to satisfy $\sigma < 0.71°$.

Both quality cuts were determined with the goal to maximize the statistical significance of the shadows in [25] and have been used in previous studies [16,26,27].

IV. DATA ANALYSIS

A. Relative coordinates

For calculating relative coordinates, the direction of each muon in the sample is compared to the known position of moon and Sun in the sky[3] using equatorial coordinates, i.e., right ascension α and declination δ.

To this end, relative right ascension $\Delta\alpha$ and relative declination $\Delta\delta$ are calculated as

$$\Delta\alpha = \alpha_\mu - \alpha_{\mathrm{Moon/Sun}} \tag{2}$$

$$\Delta\delta = \delta_\mu - \delta_{\mathrm{Moon/Sun}}, \tag{3}$$

wherein α_μ and δ_μ represent the individual reconstructed right ascension and declination of each muon event. Then, quasi-Cartesian coordinates relative to the center of the moon and Sun are determined as

$$x = \Delta\alpha \cos\delta_\mu \tag{4}$$

$$y = \Delta\delta. \tag{5}$$

B. On- and off-source regions

Based on the calculated quasi-Cartesian relative coordinates x and y, one on-source region and eight off-source regions are defined as shown in Figure 3. Each region has an angular extent of 6° × 6°, resulting in a total angular area of 54° × 6° for the nine regions.

In order to account for the spherical distortion, we keep the corrected relative right ascension $\Delta\alpha \cos\delta_\mu$ of the entire analyzed region constant at 54° rather than the uncorrected relative right ascension $\Delta\alpha$.

C. Event numbers and average declination

The number of events contained in the 54° × 6° window described in Section IV B and their average declination are given in Table I.

It can be seen that the number of events varies between 3.8 and 7.9 million events for the moon shadow sample, while it amounts to 13.1 to 13.3 million events for the Sun shadow sample, except for IC79, which contains about 9 million events.

The average declination, on the other hand, varies between −16.7° and −22.1° for the moon shadow sample and amounts to −21.8° for the Sun shadow sample, except for IC79, where it is slightly smaller with −22.1°. These values are used later for modeling the expected relative deficit due to the lunar and solar disk as described in detail in Section V C.

D. 2D maps and smoothing

After defining on- and off-source regions as described in Section IV B, the off-source regions are shifted with respect to the on-source region such that they are centered at $x = 0°$ (displayed as the black × in Figure 3), becoming directly comparable to the on-source region, which is centered at $x = 0°$ by definition.

Then, two two-dimensional binned histograms containing the number of events are defined: The first encloses the on-source region, and the second represents the average of the eight off-source regions. Both histograms cover 6° × 6° in x and y and consist of 60 × 60 bins (i, j) ($i = 1 \ldots 60$, $j = 1 \ldots 60$), wherein each bin has a size of 0.1° × 0.1°.

[2]The likelihood profile is defined as the entirety of likelihood values as a function of the directional coordinates; see [24] for details.

[3]Sky positions of the moon and Sun are calculated with IceCube-internal C++ routines using the SLALIB library [28].

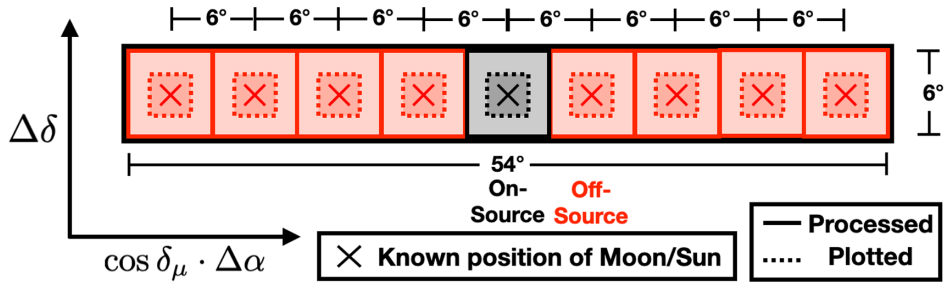

FIG. 3. On- and off-source regions used for the data analysis. The black "x" marks the zero point of the relative coordinates, i.e., the center of the moon and Sun.

Then, the relative deficit due to the shadowing of the moon and Sun in each bin (i, j) is calculated using the number of events $N_{\text{on}}^{i,j}$ in bin (i, j) in the on-source region and the average number of events $\langle N_{\text{off}}\rangle^{i,j}$ in the eight off-source regions:

$$\left(\frac{\Delta N}{\langle N_{\text{off}}\rangle}\right)^{i,j} = \frac{N_{\text{on}}^{i,j} - \langle N_{\text{off}}\rangle^{i,j}}{\langle N_{\text{off}}\rangle^{i,j}}. \tag{6}$$

The average number of events $\langle N_{\text{off}}\rangle^{i,j}$ in a bin (i, j) located in the off-source regions is calculated by averaging over the off-source regions:

$$\langle N_{\text{off}}\rangle^{i,j} = \frac{1}{8}\sum_{n=1}^{8} (N_{\text{off}}^{i,j})_n, \tag{7}$$

where $(N_{\text{off}}^{i,j})_n$ is the number of off-source events in the nth off-source region. The result is a two-dimensional map of the relative deficit due to the moon and Sun shadows.

In order to better suppress statistical fluctuations, the two-dimensional relative deficit map is smoothed with a boxcar smoothing algorithm. The smoothed relative deficit in each bin (i, j) is determined as the average of all bins whose bin centers are within a certain angular distance around the center of bin (i, j). Here, this smoothing radius is set to 0.7°, which approximately corresponds to the median angular resolution and yields a reasonable balance between angular resolution and statistical uncertainty.

TABLE I. Number of events and average declination of the data sample for each year.

		Moon		Sun	
Season	Period	$N/10^6$	$-\langle\delta\rangle/°$	$N/10^6$	$-\langle\delta\rangle/°$
2010/2011	IC79	7.9	22.1	9.0	22.1
2011/2012	IC86-1	7.7	20.7	13.1	21.8
2012/2013	IC86-2	6.4	18.9	13.1	21.8
2013/2014	IC86-3	4.5	17.7	13.2	21.8
2014/2015	IC86-4	3.8	16.9	13.2	21.8
2015/2016	IC86-5	4.1	16.7	13.3	21.8
2016/2017	IC86-6	5.1	17.2	13.3	21.8

To guide the eye, and for the numerical analysis presented in the next section, the center of gravity of the shadow is determined and plotted as well[4] (see Figs. 6 and 7). It is determined by averaging over the positions of all bins with a relative deficit of 3% or more after smoothing. As typical statistical uncertainties after the smoothing amount to about 0.6%, this threshold defines bins that show a statistically significant deficit of events.

E. Numerical analysis

In order to quantify the deficit of cosmic-ray induced muon events due to the shadowing of the moon and Sun, the relative deficit of events in a 1°-circle around the center of gravity (cf. previous section) is computed. Choosing a reasonable search radius is a trade-off between a smaller statistical error on the one hand and more off-source background contamination (washing out the deficit due to the moon and Sun) on the other hand. Within 1°, the cumulative point spread function contains about 70% of events, while the off-source background contamination is still relatively small. The statistical uncertainty of the relative deficit is computed using error propagation as

$$\sigma_{\text{RD}} = \frac{N_{\text{on}}}{\langle N_{\text{off}}\rangle}\sqrt{\frac{1}{N_{\text{on}}} + \frac{1}{s\cdot\langle N_{\text{off}}\rangle}}, \tag{8}$$

with the number of off-source regions $s = 8$.

In addition to the relative deficit, the significance of the shadowing effect is calculated using a standard formula[5] developed by Li and Ma, whereby a 0.7°-circle around the center of gravity is chosen as a search area. The selected search radius maximizes the statistical significance for very large numbers of background events and for an angular resolution typical for atmospheric muon events (cf. [25,27] for details).

[4]It should be noted that for the Sun shadow, the center of gravity is not necessarily expected to align with the center of the solar disk due to the influence of the solar magnetic field.

[5]See Eq. (17) in [29].

V. SIMULATIONS

A. Models

The simulations used for characterizing the cosmic-ray induced atmospheric muon flux are based on CORSIKA [30]. More specifically, two CORSIKA-generated simulation sets are used, covering primary energies from 600 GeV to 100 EeV and containing ^{1}H, ^{4}He, ^{14}N, ^{27}Al, and ^{56}Fe nuclei. Hadronic interactions are simulated with SIBYLL 2.1 [31] and the MSIS-E-90 atmospheric profile [32]. Lepton propagation in ice is carried out using the lepton propagation tool PROPOSAL [33]. Light emission and propagation is handled using GEANT4 [34] and the IceCube-internal software package CLSim that has been developed based on the Photonics code [35]. The Antarctic ice in which IceCube is embedded is modeled using the SPICE Lea model [36,37]. The detector response is simulated based on internal software. After simulating atmospheric muon events using the models described above, each event is weighted based on a model of the primary cosmic-ray flux: The weight w of an event induced by a primary cosmic ray with energy E, mass number A, and atomic number Z is determined as the ratio of the cosmic-ray flux Φ_{model} according to a chosen model and the simulated cosmic-ray flux Φ_{sim}:

$$w(E,A,Z) = \frac{\Phi_{\text{model}}(E,A,Z)}{\Phi_{\text{sim}}(E,A,Z)}. \tag{9}$$

Here, the model by Gaisser with an extragalactic component presented in [38] and based on the Hillas approach, thus called the HGm model hereafter, is used.

B. Sample characteristics

Based on the models described in the previous section and the data analysis presented in Section IV, the (simulated) data sample is characterized with respect to the energy distribution of primary cosmic rays (Figure 4) and the probability density function (PDF) of the opening angle $\Delta\theta$ between reconstructed muon direction and actual cosmic-ray direction (Figure 5). Both figures show the distribution of the final simulation sample after the same steps as described in Section III. The base declination δ_0 is chosen such that the $\pm 3°$ declination band around it has the same average declination as the final Sun shadow data sample (cf. [27] for more details). The simulation sample contains events with primary energies between ~1 TeV and ~100 PeV. The median energy amounts to about 60 TeV and the 68% interval is between 14.6 TeV and 302 TeV. The median angular error amounts to 0.77°, and the 68% interval covers values between 0.31° and 2.1°.

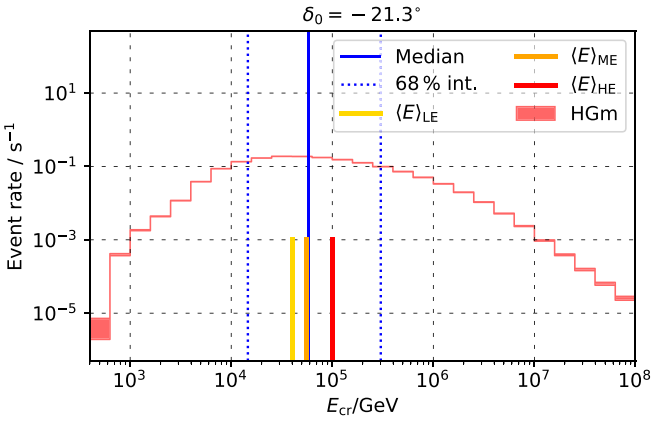

FIG. 4. Energy distribution in a $\pm 3°$ declination band around the base declination $\delta_0 = -21.3°$. The thick yellow, orange, and red lines indicate the median primary cosmic-ray energies studied in Section V G.

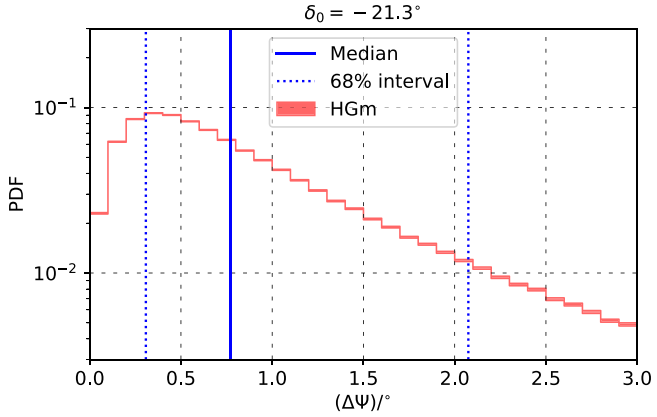

FIG. 5. Angular error distribution in a $\pm 3°$ declination band around the base declination $\delta_0 = -21.3°$.

C. Simulating the shadows

The shadowing of cosmic rays due to the moon and Sun is modeled by modifying the primary cosmic-ray weight w of each event. Using the probability p of each primary cosmic ray to pass through interplanetary space without hitting the moon or the Sun, the modified weight w' is calculated as

$$w' = p \cdot w. \tag{10}$$

In the simplest model, the moon and Sun are treated as nonmagnetic, totally absorbing spheres in space, which block those cosmic rays that come from directions within the respective lunar and solar disk as seen from Earth. In this model, p is a step function only depending on the space angle $\Delta\theta$ between the cosmic-ray direction and the center of the moon and Sun.

Although cosmic rays are deflected by the geomagnetic field, the net shadowing effect remains largely unaffected, besides a small shift of the shadow that is significantly smaller than the resolution of the detector is expected. Moreover, by applying the center-of-gravity correction presented in Section IV E before calculating the relative deficit, such a shift is accounted for in the analysis method.

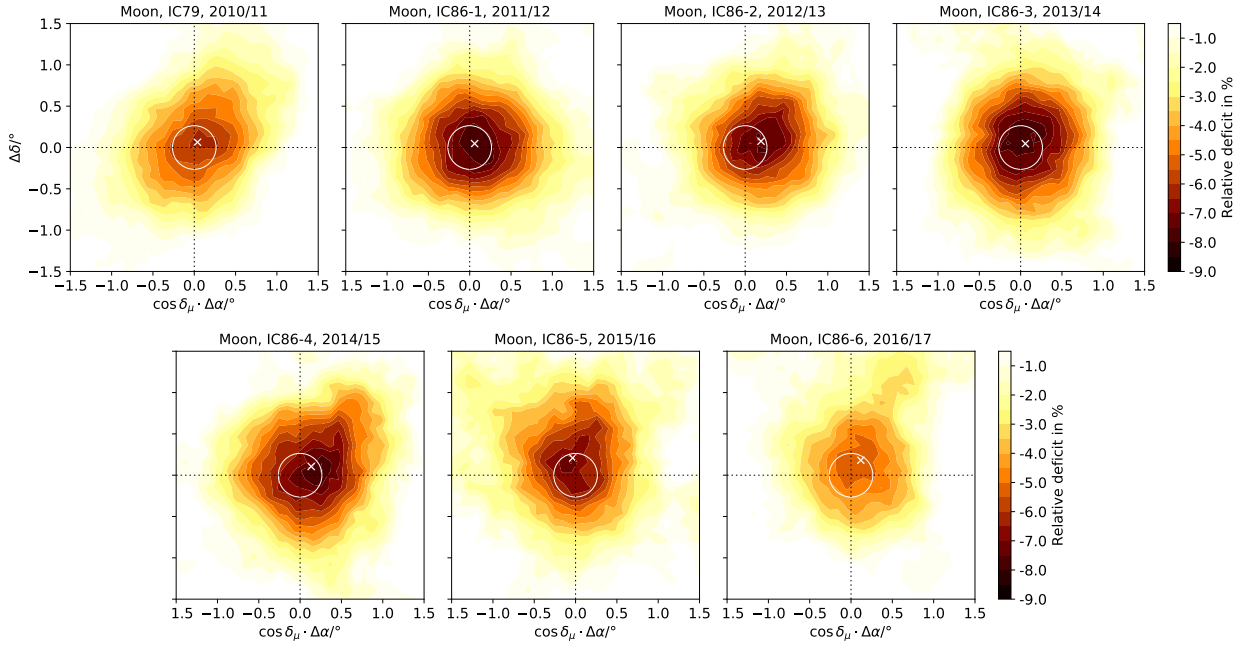

FIG. 6. Boxcar-smoothed two-dimensional contour map of the moon shadow for the years IC79 to IC86-6 showing the computed center of gravity of the shadow as a white cross. The white circle indicates the seven-year mean of the weighted average of the angular moon radius.

In order to simulate the expected relative deficit due to the lunar and solar disk, two key parameters are taken into account: the average declination $\langle\delta\rangle$ of each data sample given in Table I and the weighted average of the apparent radius $\langle R_{\mathrm{app}}^{\mathrm{Moon}/\odot}\rangle$ of the moon and Sun. While the average declination determines typical energies and the median angular resolution (cf. [27]), the apparent radius determines, in simple words, how large lunar and solar disk have to be modeled.

For calculating $\langle R_{\mathrm{app}}^{\mathrm{Moon}/\odot}\rangle$, the number of events for each Modified Julian Date (MJD), N_{MJD}, is determined together with the apparent radius in the sky for each individual MJD

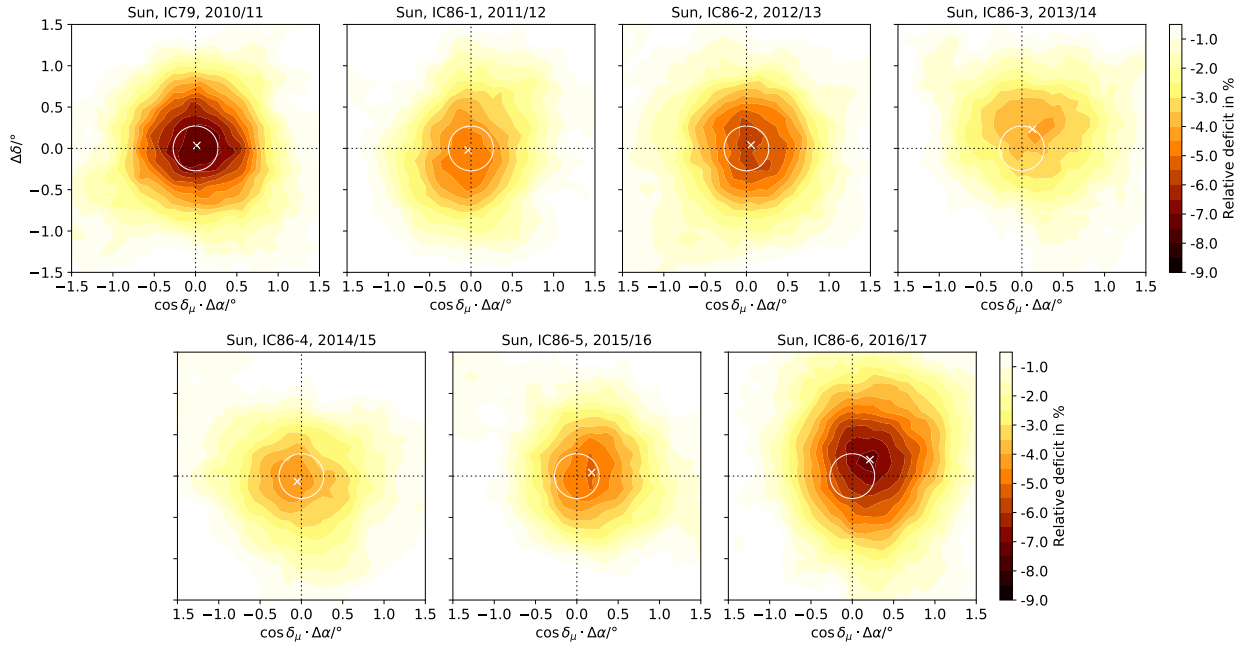

FIG. 7. Boxcar-smoothed two-dimensional contour map of the Sun shadow for the years IC79 to IC86-6 showing the computed center of gravity of the shadow as a white cross. The white circle indicates the weighted average of the angular Sun radius.

of the sample, $R_{\mathrm{app}}^{\mathrm{MJD}}$. The latter is calculated using Eq. (1) after obtaining the Earth-moon distance for that specific MJD through ASTROPY [20,21]. Using these pieces of information, the weighted apparent radius becomes

$$\langle R_{\mathrm{app}}^{\mathrm{Moon}/\odot} \rangle = \frac{\sum_{\mathrm{MJD}} N_{\mathrm{MJD}} \cdot R_{\mathrm{app}}^{\mathrm{MJD}}}{\sum_{\mathrm{MJD}} N_{\mathrm{MJD}}}. \tag{11}$$

With this procedure, the weighted average of the apparent radius of the moon in the sky is shown to vary between the 0.251° (IC86-6) and 0.274° (IC86-2).

For the Sun, the range of its apparent size varies, in general, between 0.262° and 0.271° over the year. For the time from November through February studied in this paper, however, it amounts to 0.271° for each year. As a result of neglecting the subpercent variation of this value, the expectation for the geometrical shadowing effect of the solar disk is the same in each year.

For simulating the Sun shadow, including the effect of the solar magnetic field, the picture is much more complex. Besides the geomagnetic field, the heliospheric magnetic field and especially the solar coronal magnetic field also deflect cosmic rays. While the heliospheric magnetic field, like the geomagnetic field, is comparably regular, the coronal magnetic field can become highly irregular. This increased level of magnetic small-scale variability enhances the interactions of cosmic rays with the magnetic field, thus changing the net shadowing effect of the Sun. A first quantification of how the shadowing effect is changed has been discussed in [15]. It is thus necessary to actually simulate cosmic-ray propagation in the heliospheric and coronal magnetic field. In such a simulation, the passing probability p of each primary cosmic ray can be determined. It can be calculated as the number of cases n_{pass}, in which the cosmic-ray particle traverses the solar corona without hitting the photosphere, divided by the total number of trials n_{total},

$$p = \frac{n_{\mathrm{pass}}}{n_{\mathrm{total}}}. \tag{12}$$

This implies that the solar photosphere is treated as a perfect absorber for CRs of any energy and that any interaction possibly occurring in the lower solar atmosphere [39] is neglected at this point. The shadow effect should not be changed significantly, as the secondary high-energy particles will mostly be absorbed by the Sun. The effect is rather important for neutrino measurements from the Sun: The neutrinos in cosmic-ray interactions in the solar atmosphere represent a background for dark matter searches in IceCube as early estimated by [40,41]. These neutrinos define the so-called *neutrino floor* for the dark matter searches with IceCube, as predicted in [42–44]. These most recent estimates of the neutrino flux from solar atmospheric neutrinos predict ∼1 event per year [42], ∼2–3 events per year [43], and ∼5–6 events per year [44] within IceCube, respectively. Cutting away the GeV background of neutrinos actually provides the opportunity to measure these neutrinos produced in the solar atmosphere directly, with first limits presented in [45] by searching for neutrino emission from the Sun with IceCube. For the latter analysis, the used data are complementary to the one in this analysis as for the purpose of background reduction, and only data are used when the Sun is below the horizon, while we use the data when the Sun is above the horizon at South Pole. The potential neutrino flux of ∼1 per year is negligible as compared to our signal of $\gg 10^6$ events per year.

The above probability can be calculated by propagating cosmic rays in the magnetic field of the Sun. Here, we use a backtracking approach for computing time-efficient simulations, and we perform the propagation in two different magnetic field models. The details of these parts of the simulation are described in the subsequent Sections V D and V E.

D. Particle propagation in the solar magnetic field

In order to produce simulations of the cosmic-ray shadow at Earth, the first step is to numerically propagate the particles through the magnetic field of the Sun. We use the test-particle approach, which implies that the magnetic field configuration is not changed by the particle current. This is a reasonable assumption for such high-energetic particles, whose coronal crossing time of a few minutes is much smaller than the timescales of solar magnetic variability and thus allows us to keep the magnetic field configuration constant for the simulation of one particle trajectory. Moreover, since the mean free paths of TeV particles traversing the solar corona are significantly longer than the system scales of a few solar radii to 1 AU, the usual diffusive approach (e.g., [15,46,47]) often employed in the interstellar medium is not appropriate for the present setting. Therefore, the particles are instead propagated according to the equation of motion,

$$\frac{d\vec{p}}{dt} = q(\vec{v} \times \vec{B}), \tag{13}$$

following the approach in [15]. As described in the following subsection, the simulations are performed for two magnetic field models. Thereby, the simulations are performed for different magnetic field configurations, corresponding to the solar magnetic field at different times. More precisely, 3D solar magnetic fields are generated for each month from 2D solar magnetograms and are kept constant for that month. Details of the two models and their respective implementations are described in the following section.

Propagating particles forward is very inefficient, as it cannot be defined beforehand which of these particles actually hit Earth and which do not. Thus, in order to produce a computing-time efficient simulation, only those cosmic rays that eventually induce an atmospheric muon

event in the final simulation sample are propagated. This is achieved by using a backtracking method, which takes the known primaries of the final simulation sample, changes all particles into their antiparticles, and, at the same time, inverts their momentum vector. This means that in the simulations, we start antiparticles at Earth, propagate them around the Sun, and detect the resulting projected shadow behind the Sun. Changing the charge and the direction at the same time delivers the same result as the propagation of particles along the inverted path. The backtracking method is therefore well-suited to reduce computational time while still providing a proper picture of the propagation in the magnetic field.

E. Solar magnetic field models

As mentioned before, the solar magnetic field consists of two components: the coronal magnetic field and the heliospheric magnetic field. While the coronal magnetic field is modeled using (a) a potential-field model and (b) a magnetohydrostatic model, the heliospheric magnetic field is modeled using a Parker spiral approach [48], with a piecewise-linear approximation of the radial solar wind velocity profile.

1. PFSS model

The potential-field source-surface (PFSS) model [49,50] assumes the solar corona current-free, i.e., $\vec{j} = \vec{0}$, and hence force free, with the current density $\vec{j}$. Neglecting the displacement current, $\vec{j}$ can be related to the curl of the magnetic field $\vec{B}$ as

$$\vec{j} = \frac{1}{\mu_0}(\vec{\nabla} \times \vec{B}). \tag{14}$$

For a current-free corona, the magnetic field must hence be curl free, $\vec{\nabla} \times \vec{B} = \vec{0}$, which means that it can be expressed as the gradient of a scalar potential Φ, $\vec{B} = -\nabla\Phi$. With $\vec{\nabla} \cdot \vec{B} = 0$, this yields the Laplace equation,

$$\vec{\nabla}^2\Phi = \Delta\Phi = 0. \tag{15}$$

The PFSS model uses one parameter, the source-surface radius $R_{\rm ss}$, which delimits the domain in which the magnetic field dominates the plasma. Beyond this source surface, the plasma becomes superalfvnic, and the magnetic field is passively advected outward in it. The source-surface radius is set to $R_{\rm ss} = 2.5R_\odot$, which is a commonly used value and has also been tested in [8].

For computing magnetic fields according to the above model on a 3D spherical grid extending from the photosphere up to the source surface, we used 2D magnetic flux integral synoptic maps obtained from SOLIS [51] as photospheric boundary conditions to the FDIPS code [52].

2. CSSS model

The current-sheet source-surface (CSSS) model [53] is based on the magnetohydrostatic equation,

$$\vec{0} = \vec{j} \times \vec{B} - \vec{\nabla}p + \rho\vec{g}, \tag{16}$$

which balances the Lorentz force, the gradient of the plasma pressure p, and the gravitational acceleration $\vec{g}$ that acts on the plasma density ρ.

The CSSS model is based on the solution presented in [54] and uses three parameters: the source-surface radius $R_{\rm ss}$, the cusp radius $R_{\rm cp}$, and the length scale $l_{\rm a}$ of horizontal currents. While $R_{\rm ss}$ is set to $2.5R_\odot$ and has the same meaning as in the PFSS model, $R_{\rm cp}$ is the radius where magnetic field lines become closed. $R_{\rm cp}$ is set to $1.7R_\odot$, which is a typical height for coronal streamers. Above $R_{\rm cp}$, magnetic field lines are assumed to be open. The length scale $l_{\rm a}$ of horizontal currents is set to $1R_\odot$.

As for the PFSS model, we used the 2D magnetic flux integral synoptic maps obtained from SOLIS [51] as photospheric boundary conditions. For implementing the model described in this section, however, a code written by X.P. Zhao and J.T. Hoeksema [53,55,56] based on a spherical harmonics approach was used. The order of the spherical harmonic series is set to $n = 10$, which is sufficient for describing small-scale structures that are relevant to $\gtrsim$1 TeV particles (cf. [8]).

3. Parker spiral

The heliospheric magnetic field is implemented using the model first developed by Parker [48] (cf. [57] for a review). Field lines of the Parker spiral in general have their footpoints as an inner boundary of the description of the field, which, for the Sun, is typically assumed to be the coronal base [57], and from which, field lines start out radially. Since both the PFSS and CSSS model enforce exactly such radial field lines at the source surface $R_{\rm ss}$, it is natural to identify the latter with said coronal base used in the Parker spiral. While the magnetic field at the footpoints of the Parker spiral is determined using the coronal models described above, the three components of the Parker spiral magnetic field beyond the coronal base are computed using equations (1), (3), and (4) from [57]. This allows us to continue the computed magnetic field solution toward lager radii in a way that not only ensures conservation of magnetic flux across the source surface, but also avoids the use of inappropriate simplifications, such as a global tilt angle of the magnetic equator [58], which would not be a meaningful concept for the complex polarity distributions arising from magnetograms. The radial velocity V_r of the solar wind, which, in the frozen-magnetic-flux model, determines the azimuthal component of the magnetic field, is modeled as a piecewise-linear approximation of the Parker [48] isothermal solar wind profile:

$$V_r(r) = \begin{cases} C \cdot (r/R_\odot) & r < R_c \\ V_0 & r \geq R_c, \end{cases} \quad (17)$$

with the slope $C = V_0 \cdot (R_\odot/R_c) = 20\ \mathrm{km\,s^{-1}}$ and the critical radius $R_c = 22.5 R_\odot$. Beyond R_c, the radial velocity is assumed constant with a value of $V_0 = 450\ \mathrm{km\,s^{-1}}$, which is a typical value for the radial solar wind velocity at 1 ua (cf. [57]).

F. Coordinate transformation for signal simulation

For a proper description of the propagation, coordinates need to be transformed into ecliptic coordinates before starting the propagation around the Sun, which adds an additional transformation step. The relative coordinates with respect to the Sun's position, $\Delta\lambda$ and $\Delta\beta$, are given by

$$\Delta\lambda = \lambda_{cr} - \lambda_\odot \quad (18)$$

$$\Delta\beta = \beta_{cr} - \beta_\odot, \quad (19)$$

with $(\lambda_\odot, \beta_\odot)$ as the position of the Sun in ecliptic coordinates and $(\lambda_{cr}, \beta_{cr})$ as the position of the detected cosmic ray in ecliptic coordinates. These relative coordinates can then be transformed into quasi-Cartesian coordinates as follows:

$$x' = \cos\beta_{cr} \cdot \Delta\lambda \quad (20)$$

$$y' = \Delta\beta. \quad (21)$$

Here, x' is corrected for the spherical distortion by the $\cos\beta_{cr}$ factor, just as it is done for the moon in equatorial coordinates. While Earth's axial tilt of about 23.4° is taken into account by transforming from equatorial to ecliptic coordinates, the tilt of the Suns rotational (and magnetic) axis with respect to the ecliptic of about 7.25° is neglected in this approach, as it is significantly smaller than the Earth's axial tilt with respect to the ecliptic. Finally, the coordinates are transformed back into the equatorial system that is used for the data analysis of moon and Sun and also for the simulation of the moon data.

G. Energy reconstruction

For studying the cosmic-ray Sun shadow at different energies, the data are divided into three energy bands. This is achieved by using an energy-correlated observable, q_{dir}, which represents the charge deposited in direct hits. These direct hits are defined as not having undergone significant scattering in the ice from the point of their emission, thus providing more accurate timing information. For the observable q_{dir}, the sum of charge deposited in all DOMs that are hit within a time window of (−15 ns, 75 ns) around the first geometrically possible arrival of a Cherenkov photon in a DOM is given in units of photoelectrons (PE).

TABLE II. Summary of the parameters for the three energy bins of the analysis.

q_{dir}/PE	range (68%)/TeV	E_{median}/TeV
<18	(12–160)	40
18–30	(15–260)	55
>30	(21–630)	100

The three bins are defined as $q_{dir} < 18$ PE, $18 \leq q_{dir} \leq 30$ PE, and $q_{dir} > 30$ PE, resulting in an approximately equal number of events in each energy bin; see Table II for details. These three subsamples have median primary energies of 40 TeV, 55 TeV, and 100 TeV as shown in Figure 4.

VI. RESULTS

A. Shadow maps

The shadow maps for the moon and the Sun as a result of this analysis are presented here for each IceCube season. Figure 6 shows the cosmic-ray shadow of the moon. Each panel shows one year of data, starting with the earliest season 2010/2011 (IC79) on the top left, followed by data for the seasons 2011/2012 (IC86-1), 2012/2013 (IC86-2), and 2013/2014 (IC86-3) in the top row, and 2014/2015 (IC86-4), 2015/2016 (IC86-5), and 2016/2017 (IC86-6) in the bottom row from the left to the right. Data have been smoothed with the boxcar average algorithm, where the smoothed relative deficit in each bin (i, j) is determined as the average of all bins with centers within a certain angular distance around the center of bin (i, j). Here, this smoothing radius is set to 0.7°, which approximately corresponds to the median angular resolution of the simulation sample and yields a reasonable balance between angular resolution and statistical uncertainty (cf. Section IV D).

The figure shows that the relative deficit reaches a depth larger than 8.0%. Figure 7 shows the corresponding pictures for the location of the Sun.

The significance of the shadowing effect (cf. Section IV E) is found to fall between 7.5σ and 14.2σ for the moon and between approximately 9.5σ and 16.9σ for the Sun (see Table III). The reason for the higher significance of the Sun shadow is its larger data sample. An interpretation of these figures, and, in particular, a quantification of a possible temporal change in the shadow, will be given in the next section.

B. Comparison to lunar/solar disk

As described in Section IV E, the relative deficit within a 1.0°-circle around the center of gravity of the shadow is used for quantifying the deficit of cosmic-ray induced muon events due to the moon and Sun shadows. Figures 8–11, 13, 14 thus use this quantity. In Figure 8, the

TABLE III. Relative deficit (RD) and Li-Ma significance S (cf. Section IV E) for the moon and Sun shadows.

		2010/2011 IC79	2011/2012 IC86-1	2012/2013 IC86-2	2013/2014 IC86-3	2014/2015 IC86-4	2015/2016 IC86-5	2016/2017 IC86-6
Moon	RD in %	4.0 ± 0.4	5.0 ± 0.4	4.5 ± 0.4	5.6 ± 0.5	5.3 ± 0.6	4.9 ± 0.6	3.7 ± 0.5
	S in σ	11.2	14.2	12.1	10.0	9.4	9.5	7.5
Sun	RD in %	5.1 ± 0.4	3.3 ± 0.3	4.1 ± 0.3	3.1 ± 0.3	2.8 ± 0.3	3.5 ± 0.3	5.2 ± 0.3
	S in σ	14.0	11.4	13.0	9.5	10.1	12.1	16.9

observed relative deficit due to the cosmic-ray moon shadow is compared to the relative deficit expected due to geometrical shadowing of the moon. The simulations show the same slight dip as the data. The reason for this dip is the slightly different distance between moon and Earth, which changes the angular radius and hence, the shadowed solid angle. Additionally, the average declination of the event sample is slightly different for each year. Both effects are accounted for in the simulations shown in Figure 8.

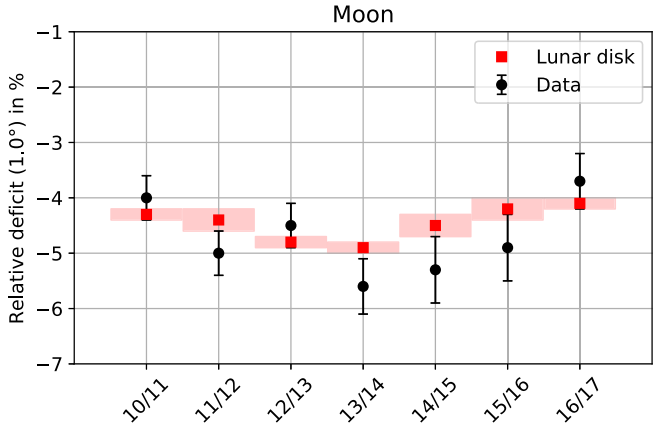

FIG. 8. Comparison of measured relative deficit due to the moon shadow (black circles) and relative deficit expected from shadowing by the lunar disk (red squares).

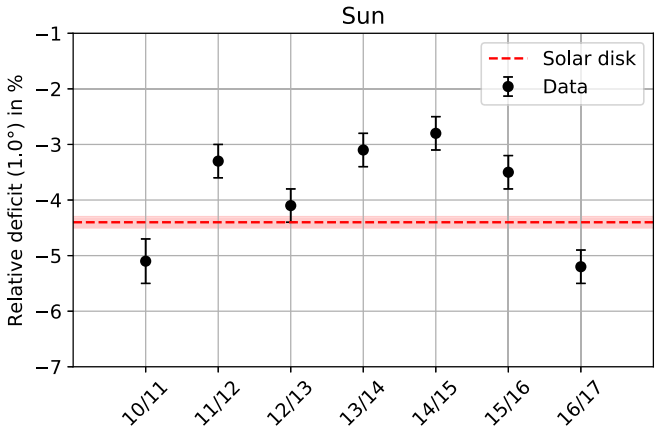

FIG. 9. Comparison of measured relative deficit due to the Sun shadow and relative deficit expected from shadowing by the solar disk.

In Figure 9, the observed relative deficit due to the cosmic-ray Sun shadow is compared to the relative deficit expected due to geometrical shadowing of the Sun. There is no substantial variation in the distance between Sun and Earth for the observation period November through February. Also, the average declination of the data sample is essentially the same each year. Thus, the expected relative deficit due to the geometrical shadowing by the solar disk is the same every year and amounts to $(4.4 \pm 0.1)\%$.

In order to statistically quantify the agreement between measured and expected relative deficits shown in Figs. 8 and 9, a χ^2-test is performed. To this end, the χ^2 between the data points x^i_{data} and the simulated data points x^i_{sim} is calculated as

$$\chi^2 = \sum_i \frac{(x^i_{\text{data}} - x^i_{\text{sim}})^2}{(\sigma^i_{\text{data}})^2}, \tag{22}$$

with the statistical uncertainty σ^i_{data} of each data point. Then, using the calculated χ^2 and the number of degrees of freedom n_{dof}, the p value is calculated from the cumulative distribution function of the appropriate χ^2-distribution. Here, the number of degrees of freedom corresponds to the number of data points, $n_{\text{dof}} = 7$. As in [16,25], the significance S is then calculated as

$$S = \sqrt{2}\text{erf}^{-1}(1 - p), \tag{23}$$

with the inverse error function erf^{-1}.

In Table IV, the reduced χ^2, p value, significance S of a χ^2 test of the observed moon and Sun shadows, and the expectation from the lunar and solar disk are given. With a p value of 32%, the moon shadow shows reasonable agreement with the expectation from the lunar disk. The Sun shadow, on the other hand, is incompatible with the expectation from the solar disk with a statistical significance of about 7 standard deviations.

TABLE IV. Reduced χ^2, p value, and significance of the comparison to the lunar and solar disk.

	χ^2/n_{dof}	p	S in σ
Moon	$8.2/7 \approx 1.2$	0.32	1.0
Sun	$72.9/7 \approx 10.4$	3.9×10^{-13}	7.3

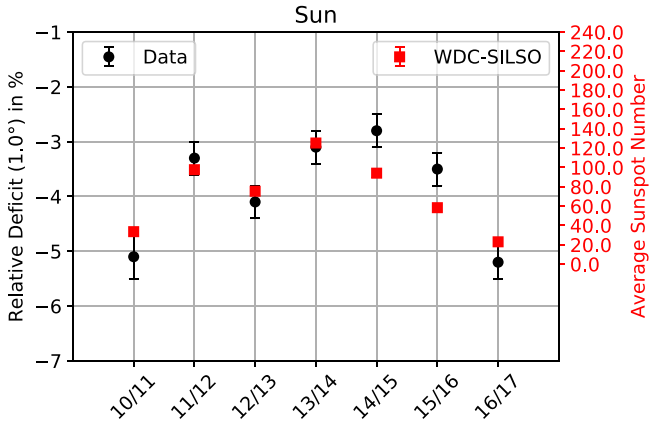

FIG. 10. Comparison of measured relative deficit due to the Sun shadow and average sunspot number as a tracer for solar activity.

C. Comparison to solar cycle

As a first observational test of a connection between magnetic solar activity and the Sun shadow, the temporal variation of the cosmic-ray Sun shadow is compared to the average *International Sunspot Number* obtained from [59]. A similar comparison has already been performed in [16] for five years of data, and a correlation has been found to be likely. In Figure 10, the relative deficit due to the Sun shadow is shown together with the sunspot number (averaged over the relevant months) between November 2010 and February 2017.

In order to quantify the correlation between Sun shadow and solar activity, which is shown in Figure 11, two correlation tests are performed. The results of these tests are summarized in Table V. While a Spearman's rank correlation test yields a correlation coefficient of 0.86 and a p value of 1.4% for a correlation by chance, a Kendall-τ test yields a correlation coefficient of 0.71 and a p value of 3.0%.

We also quantify the deviation from a constant function by fitting a linear function and a constant one. We calculate

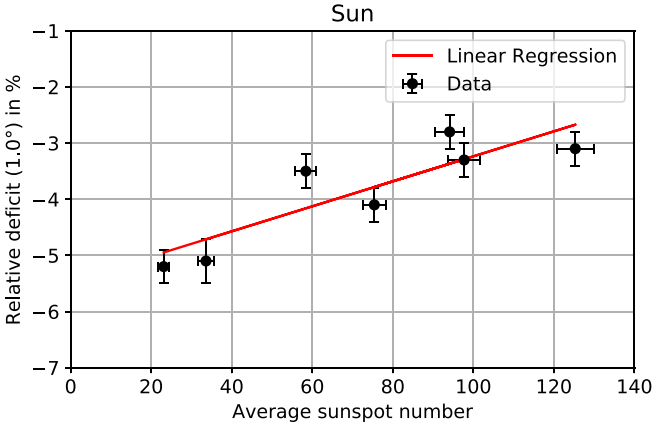

FIG. 11. Correlation of measured relative deficit due to the Sun shadow and average sunspot number. A correlation of the two quantities is found to be likely.

TABLE V. Correlation coefficient and p value of the two performed correlation tests.

Correlation test	Correlation coefficient	p in %
Spearman's ρ	0.86	1.4
Kendall's τ	0.71	3.0

the difference in the χ^2 and number of degrees of freedom, $\Delta\chi^2$ and Δn_{dof}, respectively. Based on these values, the p value is calculated from the cumulative distribution function of the appropriate χ^2 distribution. While we find $\chi/n_{\mathrm{dof}} = 13.23/5$ for the linear model, the constant model yields $\chi/n_{\mathrm{dof}} = 53.67/6$. The difference in these two models therefore can be quantified to

$$\frac{\Delta\chi^2}{\Delta n_{\mathrm{dof}}} = \frac{40.44}{1} = 40.44. \tag{24}$$

This results in a p value of $p = 2.0 \times 10^{-10}$, corresponding to a significance of 6.4σ that the linear fit is preferred over a constant one.

Finally, we also show the moon shadow normalized to the simulated shadow from geometrical shadowing as a function of the average sunspot number in Fig. 12. The result can be fitted by a constant with a $\chi^2/n_{\mathrm{dof}} = 1.286$. This confirms that the moon is well-described by geometrical shadowing.

D. Comparison to solar magnetic field models

Finally, we modeled cosmic-ray propagation in the solar magnetic field to obtain predictions for the Sun shadow as expected from different coronal magnetic field models. Figure 13 shows the results in terms of the observed relative deficit due to the Sun shadow and the expected relative deficit based on the PFSS and CSSS models in combination with the Parker spiral model introduced in Section V E.

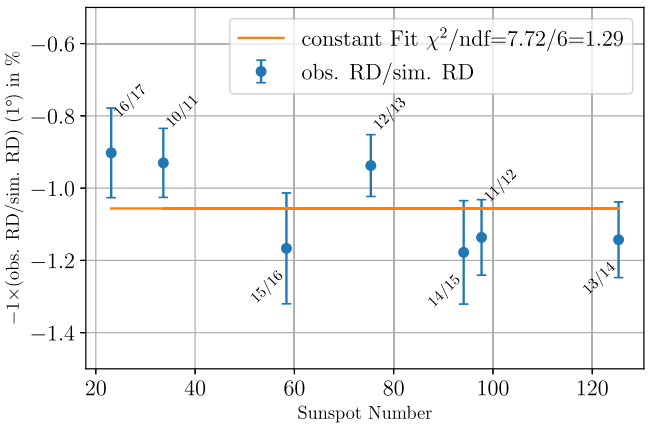

FIG. 12. Normalized moon shadow deficit versus sunspot number.

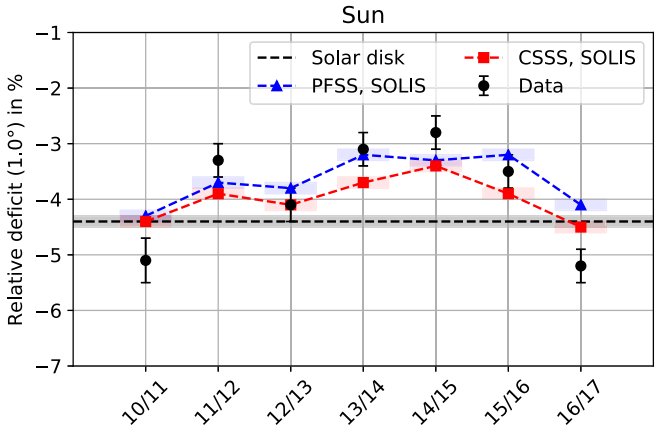

FIG. 13. Comparison of measured relative deficit due to the Sun shadow and relative deficit expected from different models of the solar magnetic field.

Both models reproduce the observed weakening of the shadow in times of high solar activity. The PFSS model predicts a more pronounced weakening of the shadow than the CSSS model in all years that are studied. In 2010/2011, as well as in 2016/2017, the relative deficit observed in the data is slightly stronger than the prediction from both models but also stronger than the expectation from the solar disk. In addition to a χ^2 test taking into account the statistical uncertainties of the data points, a modified χ^2 test, which also takes into account the statistical uncertainties of the simulations and an estimate of the systematic uncertainty, is performed:

$$\chi^2 = \sum_i \frac{(x^i_{\text{data}} - x^i_{\text{sim}})^2}{(\sigma^i_{\text{data}})^2 + (\sigma^i_{\text{sim}})^2 + \sigma^2_{\text{sys}}}. \tag{25}$$

As in [8], the systematic uncertainty is estimated from comparing the observed and expected relative deficit due to the moon shadow and is found to amount to about 0.3%.

While the standard χ^2 test yields tensions between the data and the models on the order of 3 standard deviations, the modified test yields reasonable agreement with p values of 13% and 17% for the PFSS and CSSS model, respectively. All values are given in Table VI. These results can be compared to the findings of Tibet AS-γ in [8], who performed a similar study for the previous solar cycle (1996–2009) at lower energies of ∼10 TeV. In [8], it is discussed that the simulations with the CSSS model produce results that are consistent with the data. At these energies, the discrepancy with the PFSS model is larger (p value of 4.9×10^{-5}). In this paper, the CSSS model also fits somewhat better than the PFSS model, but these differences are not significant. This is the statement we can make within the present statistical uncertainties. Given the fact that Tibet's results show potential tensions on a similar significance level, we are quite confident that this is most likely not due to systematic uncertainties. In order to fully rule this out, it will be useful to compare more observations from different detectors and the same solar cycles in the future. One reason could be that the magnetic activity in Solar Cycle 24, which is investigated in this paper, is much less pronounced compared to Solar Cycle 23, which was investigated with Tibet AS-γ data. In addition, effects should be amplified at lower energies as lower-energy particles have smaller gyro radii and therefore react stronger to the magnetic field. As can also be seen in Fig. 13, our data and its analysis indicate the shadow's tendency to be weaker (stronger) than the geometrical limit during phases of high (low) solar activity, consistent with what was previously found by, e.g., the Tibet group [8]. One might speculate that this behavior is possibly caused by the stronger maximum field being able to deflect particles away from Earth more efficiently. However, since the same effect would also cause more particles to be deflected towards the observer and make them appear to originate from the solar disk, the net effect on the shadow as a whole seems inconclusive at this point. Indeed, it seems well conceivable that the solar cycle influences the shadow deficit not so much through variations in absolute field strength but rather through the transition from the large-scale symmetric dipolar field at solar minimum to the more irregular small-scale field prevailing at times of solar maximum. Another effect that could contribute to this tension would be the change of intensity by taking into account a gradual change in the density rather than treating the Sun as a perfect absorber. Finally, in this paper, we investigate seven years, while Tibet AS-γ could make use of 14 years of data.

E. Energy dependence

In this section, we discuss the energy dependence of the Sun shadow. In Figure 14, the relative deficit, normalized to the expectation from the solar disk, is shown for the low-energy (median energy: ∼40 TeV) and high-energy

TABLE VI. Reduced χ^2, p value, and significance of the comparison between the measured Sun shadows and the two different models. Both models were provided with SOLIS magnetogram data [51]. Values in parentheses are based on the modified χ^2 given in equation (25).

Magnetogram	Coronal model	χ^2/n_{dof}	p	S in σ
SOLIS	PFSS	3.1 (1.6)	0.0027 (0.13)	3.0 (1.5)
SOLIS	CSSS	2.9 (1.5)	0.0052 (0.17)	2.8 (1.4)

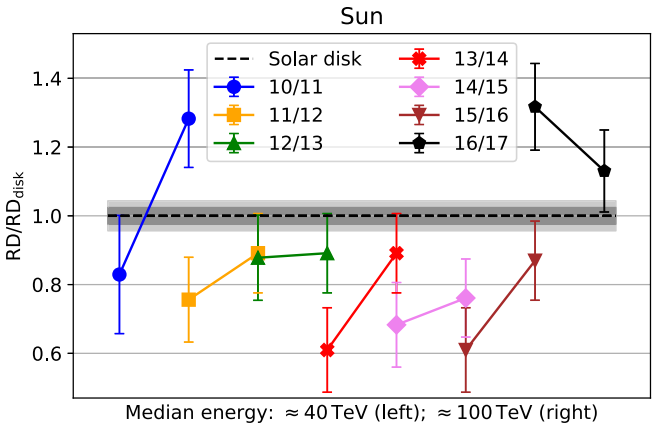

FIG. 14. Relative deficit due to the Sun shadow normalized to the expectation from the solar disk as a function of the median energy of the subsamples. For better visualization, pairs of data points for a specific season where shifted along the abscissa. The inner (outer) gray band indicates the statistical uncertainty of the disk-prediction for the low-energy (high-energy) sample.

(median energy: ∼100 TeV) subsamples during the observation period from November 2010 through February 2017. Normalizing to the solar disk is necessary as the PSF is energy dependent, causing the solar-disk shadow to be stronger for higher energies.

For years with rather high solar activity (2011/2012–2015/2016), there is a clear indication for shadow strength increasing with energy. For the two low-solar-activity years (2010/2011 and 2016/2017), no conclusions can be drawn. In general, these results are consistent with what is expected from theory [15], where it is shown that the shadow should decrease in strength for years of high level of solar activity and that it should be increasing for low-activity years. Furthermore, simulations using a pure dipole field found the shadow depth to depend nonmonotonously on rigidity, with high (low) rigidities causing shadow deficits above (below) the geometrical limit [15]. However, to confirm such trends, a better energy resolution and a larger data set are necessary; therefore, we refer to future work to investigate this question in more detail.

VII. CONCLUSION

In this paper, the time-dependent cosmic-ray moon and Sun shadows were studied using seven years of IceCube data taken between May 2010 and May 2017. Both, moon and Sun shadows are observed with high statistical significance in all seven years of data. While the moon shadow is described reasonably well by the lunar-disk model ($p = 0.32$), the Sun shadow is statistically incompatible with geometrical shadowing only due to the solar disk (7.3σ).

We compared the temporal variation of the measured relative deficit of the Sun shadow to the change in the International Sunspot Number as a tracer for solar magnetic activity. We find the probability to observe the measured correlation by chance to be 3.0% (Kendall's τ test) or 1.4% (Spearman's rank test), respectively. A linear relationship between shadow strength and solar activity is preferred over a constant one with 6.4σ.

We test two coronal magnetic field models, the PFSS and CSSS models, together with a Parker spiral beyond 2.5 solar radii. Taking into account only statistical uncertainties, we find tensions between data and models on the order of $\sim 3\sigma$. Including an estimate of the systematic uncertainty based on the observed moon shadow, however, we compute reasonable p values of 13% and 17% for the two models, respectively.

In times of high solar activity, the measured Sun shadow seems to increase with energy (1.8σ indication). In times of low solar activity, more data and an improved energy estimation will be necessary. Due to the long solar minimum of Cycle 24, the upcoming years of IceCube data will shed more light on this state in the future.

Future possibilities furthermore include testing different coronal magnetic field models like more general force-free or MHD models, studying the influence of CMEs on the Sun shadow or implementing different models of the heliospheric magnetic field and/or the radial wind velocity profile. Further, in the future, energy dependence can help to understand the strength of the field in particular when studying years of low solar activity. Here, an approximation by a Parker spiral is motivated by theory [15,60]. A dipole-type field shows an increase of the shadow depth up to a certain maximum, which has a larger shadowing effect than the geometrical shadow. The predicted behavior of the Sun shadow during low solar activity with increasing energy is a monotonous increase of the shadow, converging toward the geometrical shadow, thus, for all energies below convergence showing a shadow that is weaker than the geometrical one. Thus, for low activity years in particular, the observed peak energy can reveal the true normalization of the dipole, while the high activity years can help to disentangle the role of the small-scale component of the field.

ACKNOWLEDGMENTS

USA—U.S. National Science Foundation-Office of Polar Programs, U.S. National Science Foundation-Physics Division, Wisconsin Alumni Research Foundation, Center for High Throughput Computing (CHTC) at the University of Wisconsin-Madison, Open Science Grid (OSG), Extreme Science and Engineering Discovery Environment (XSEDE), U.S. Department of Energy-National Energy Research Scientific Computing Center, Particle astrophysics research computing center at the University of Maryland, Institute for Cyber-Enabled Research at Michigan State University, and Astroparticle physics computational facility at Marquette University; Belgium—Funds for Scientific Research

(FRS-FNRS and FWO), FWO Odysseus and Big Science programmes, and Belgian Federal Science Policy Office (Belspo); Germany—Bundesministerium für Bildung und Forschung (BMBF), Deutsche Forschungsgemeinschaft (DFG), Helmholtz Alliance for Astroparticle Physics (HAP), Initiative and Networking Fund of the Helmholtz Association, Deutsches Elektronen Synchrotron (DESY), and High Performance Computing cluster of the RWTH Aachen; Sweden—Swedish Research Council, Swedish Polar Research Secretariat, Swedish National Infrastructure for Computing (SNIC), and Knut and Alice Wallenberg Foundation; Australia—Australian Research Council; Canada—Natural Sciences and Engineering Research Council of Canada, Calcul Québec, Compute Ontario, Canada Foundation for Innovation, WestGrid, and Compute Canada; Denmark—Villum Fonden, Danish National Research Foundation (DNRF), Carlsberg Foundation; New Zealand—Marsden Fund; Japan—Japan Society for Promotion of Science (JSPS) and Institute for Global Prominent Research (IGPR) of Chiba University; Korea—National Research Foundation of Korea (NRF); Switzerland—Swiss National Science Foundation (SNSF); United Kingdom—Department of Physics, University of Oxford. The IceCube collaboration acknowledges the significant contributions to this manuscript from Frederik Tenholt (Ruhr-Universität Bochum).

[1] G. W. Clark, Arrival directions of cosmic-ray air showers from the Northern Sky, Phys. Rev. **108**, 450 (1957).
[2] M. Amenomori *et al.* (Tibet ASγ Collaboration), Cosmic ray shadow by the Moon observed with the Tibet air shower array, in *Proceedings of the 23th International Cosmic Ray Conference (ICRC1993)* (1993), Vol. 4, p. 351.
[3] W. W. Allison *et al.* (Soudan2 Collaboration), Cosmic ray sun shadow in Soudan 2 underground muon flux, in *Proceedings of the 26th International Cosmic Ray Conference (ICRC1999)* (1999), Vol. 7, p. 226.
[4] M. Ambrossio *et al.* (MACRO Collaboration), Observation of the shadowing of cosmic rays by the Moon using a deep underground detector, Phys. Rev. D **59**, 012003 (1998).
[5] F. W. Samuelson (for the Soudan2 Collaboration), The cosmic ray Moon shadow seen by MILAGRO, in *Proceedings of the 27th International Cosmic Ray Conference (ICRC2001)* (2001), Vol. 2, p. 594.
[6] B. Bartoli *et al.* (ARGO-YBJ Collaboration), Observation of the cosmic ray moon shadowing effect with the ARGO-YBJ experiment, Phys. Rev. D **84**, 022003 (2011).
[7] M. G. Aartsen *et al.* (IceCube Collaboration), Observation of the cosmic-ray shadow of the Moon with IceCube, Phys. Rev. D **89**, 102004 (2014).
[8] M. Amenomori *et al.* (Tibet ASγ Collaboration), Probe of the Solar Magnetic Field Using the "Cosmic-Ray Shadow" of the Sun, Phys. Rev. Lett. **111**, 011101 (2013).
[9] M. Amenomori *et al.* (Tibet ASγ Collaboration), Influence of Earth-directed coronal mass ejections on the Sun's shadow observed by the Tibet-III air shower array, Astrophys. J. **860**, 13 (2018).
[10] X. Xu (for the MILAGRO Collaboration), The cosmic ray shadows of the Moon and the Sun detected by the Milagro gamma ray observatory, in *Proceedings of the 28th International Cosmic Ray Conference (ICRC2003)* (2003), Vol. 7, p. 4065.
[11] G. Aielli *et al.* (ARGO-YBJ Collaboration), Mean interplanetary magnetic field measurement using the ARGO-YBJ Experiment, Astrophys. J. **729**, 113 (2011).
[12] O. Enriquez (for the HAWC Collaboration), The Galactic cosmic-ray Sun shadow observed by HAWC, *Proc. Sci.*, ICRC2015 (2016) 099 [arXiv:1508.07351].
[13] H. Porsche, HELIOS mission: Mission objectives, mission verification, selected results, in *Solar System and Its Exploration* (ESA Special Publication, 1981), p. 43.
[14] NASA, Parker Solar Probe (2019), http://parkersolarprobe.jhuapl.edu/index.php.
[15] J. Becker Tjus, P. Desiati, N. Döpper, H. Fichtner, J. Kleimann, M. Kroll, and F. Tenholt, Cosmic-ray propagation around the Sun: Investigating the influence of the solar magnetic field on the cosmic-ray Sun shadow, Astron. Astrophys. **633**, A83 (2020).
[16] M. G. Aartsen *et al.* (IceCube Collaboration), Detection of the temporal variation of the Sun's cosmic ray shadow with the IceCube detector, Astrophys. J. **872**, 133 (2019).
[17] M. G. Aartsen *et al.* (IceCube Collaboration), The IceCube neutrino observatory: Instrumentation and online systems, J. Instrum. **12**, P03012 (2017).
[18] F. Halzen, IceCube Science, J. Phys. Conf. Ser. **171**, 012014 (2009).
[19] H. Karttunen, P. Kröger, H. Oja, M. Poutanen, and K. J. Donner, *Fundamental Astronomy* (Springer, New York, 2007).
[20] T. P. Robitaille, E. J. Tollerud *et al.* (Astropy Collaboration), Astropy: A community Python package for astronomy, Astron. Astrophys. **558**, A33 (2013).
[21] A. M. Price-Whelan, B. M. Sipőcz *et al.* (Astropy Collaboration), Binary companions of evolved stars in APOGEE DR14: Search method and catalog of ∼5000 companions, Astron. J. **156**, 18 (2018).
[22] E. Tollerud, S. P. P. Nair, J. Woillez, T. Jenness, D. Terrett, O. Streicher, M. van Kerkwijk, and M. Droettboom, Essential routines for fundamental astronomy, https://doi.org/10.5281/zenodo.1021149 (2017).
[23] J. Ahrens *et al.* (AMANDA Collaboration), Muon track reconstruction and data selection techniques in AMANDA, Nucl. Instrum. Methods Phys. Res., Sect. A **524**, 169 (2004).

[24] T. Neunhffer, Estimating the angular resolution of tracks in neutrino telescopes based on a likelihood analysis, Astropart. Phys. **25**, 220 (2006).
[25] F. Bos, Studying moon and sun shadows by using atmospheric muons detected with IceCube, Ph.D. thesis, Ruhr-Universität Bochum, 2017.
[26] F. Tenholt, J. Becker Tjus, and P. Desiati (for the IceCube Collaboration), Studying the Temporal Variation of the Cosmic-Ray Sun Shadow Using IceCube Data, in *Proceedings of the 36th International Cosmic Ray Conference (ICRC2019)* (2019), https://pos.sissa.it/358/437/.
[27] F. Tenholt, Studying the temporal variation of the cosmic-ray Sun shadow, Ph. D. thesis, Ruhr-Universität Bochum, 2020.
[28] P. T. Wallace, The SLALIB Library, https://ui.adsabs.harvard.edu/abs/1994ASPC...61..481W (2020).
[29] T.-P. Li and Y.-Q. Ma, Analysis methods for results in gamma-ray astronomy, Astrophys. J. **272**, 317 (1983).
[30] D. Heck, J. Knapp, J. N. Capdevielle, G. Schatz, and T. Thouw, CORSIKA: A Monte Carlo code to simulate extensive air showers, Technical Report, Forschungszentrum Karlsruhe, 1998, fZKA 6019.
[31] E.-J. Ahn, R. Engel, T. K. Gaisser, P. Lipari, and T. Stanev, Cosmic ray interaction event generator SIBYLL 2.1, Phys. Rev. D **80**, 094003 (2009).
[32] Community Coordinated Modeling Center (CCMC), MSIS-E-90 Atmosphere Model (2019), https://ccmc.gsfc.nasa.gov/modelweb/models/msis_vitmo.php.
[33] J. H. Koehne, K. Frantzen, M. Schmitz, T. Fuchs, W. Rhode, D. Chirkin, and J. Becker Tjus, PROPOSAL: A tool for propagation of charged leptons, Comput. Phys. Commun. **184**, 2070 (2013).
[34] S. Agostinelli *et al.* (Geant4 Collaboration), GEANT4—A simulation toolkit, Nucl. Instrum. Methods Phys. Res., Sect. A **506**, 250 (2003).
[35] J. Lundberg, P. Miocinovic, K. Woschnagg, T. Burgess, J. Adams, S. Hundertmark, P. Desiati, and P. Niessen, Light tracking through ice and water–Scattering and absorption in heterogeneous media with Photonics, Nucl. Instrum. Methods Phys. Res., Sect. A **581**, 619 (2007).
[36] M. Aartsen *et al.* (IceCube Collaboration), Measurement of South Pole ice transparency with the IceCube LED calibration system, Nucl. Instrum. Methods Phys. Res., Sect. A **711**, 73 (2013).
[37] D. Chirkin (for the IceCube Collaboration), Evidence of optical anisotropy of the South Pole ice, in *Proceedings of the 33th International Cosmic Ray Conference (ICRC2013)* (2013), p. 0580.
[38] T. K. Gaisser, Spectrum of cosmic-ray nucleons, kaon production, and the atmospheric muon charge ratio, Astropart. Phys. **35**, 801 (2012).
[39] D. Seckel, T. Stanev, and T. K. Gaisser Signatures of cosmic-ray interactions on the solar surface, Astrophys. J. **382**, 652 (1991).
[40] G. Ingelman and M. Thunman, High energy neutrino production by cosmic ray interactions in the Sun, Phys. Rev. D **54**, 4385 (1996).
[41] C. Hettlage and K. Mannheim, Neutrino flux bounds and prospects for high energy and ultrahigh energy neutrino source detection, arXiv:astro-ph/0202074.
[42] C. A. A. G. de Wasseige, A. Fedynitch, and B. J. P. Jones, Neutrino flux bounds and prospects for high energy and ultrahigh energy neutrino source detection, J. Cosmol. Astropart. Phys. 07 (2017) 024.
[43] J. Edsjö, J. Elevant, R. Enberg, and C. Niblaeus, Neutrinos from cosmic ray interactions in the Sun, J. Cosmol. Astropart. Phys. 06 (2017) 033.
[44] K. C. Y. Ng, J. F. Beacom, A. H. G. Peter, and C. Rott, Solar atmospheric neutrinos: A new neutrino floor for dark matter searches, Phys. Rev. D **96**, 103006 (2017).
[45] M. Aartsen *et al.* (IceCube Collaboration), Searches for neutrinos from cosmic-ray interactions in the Sun using seven years of IceCube data, arXiv:1912.13135.
[46] M. S. Potgieter, Solar modulation of cosmic rays, Living Rev. Solar Phys. **10**, 3 (2013).
[47] P. Lipari, The lifetime of cosmic rays in the Milky Way, arXiv:1407.5223.
[48] E. N. Parker, Dynamics of the interplanetary gas and magnetic fields, Astrophys. J. **128**, 664 (1958).
[49] K. H. Schatten, J. M. Wilcox, and N. F. Ness, A model of interplanetary and coronal magnetic fields, Sol. Phys. **6**, 442 (1969).
[50] M. D. Altschuler and G. Newkirk, Magnetic fields and the structure of the solar corona, Sol. Phys. **9**, 131 (1969).
[51] National Solar Observatory, SOLIS magnetograms (2020), https://solis.nso.edu/0/vsm/vsm_maps.php.
[52] G. Tóth, B. van der Holst, and Z. Huang, Obtaining potential field solution with spherical harmonics and finite differences, Astrophys. J. **732**, 102 (2011).
[53] X. Zhao and J. T. Hoeksema, Prediction of the interplanetary magnetic field strength, J. Geophys. Res.-Space **100**, 19 (1995).
[54] T. J. Bogdan and B. C. Low, The three-dimensional structure of magnetostatic atmospheres. II—Modeling the large-scale corona, Astrophys. J. **306**, 271 (1986).
[55] X. P. Zhao, J. T. Hoeksema, and N. B. Rich, Modeling the radial variation of coronal streamer belts during sunspot ascending phase, Adv. Space Res. **29**, 411 (2002).
[56] X. P. Zhao and J. T. Hoeksema, A software package for the computation of magnetic fields in the corona and heliosphere on the basis of observed photospheric magnetic fields, http://sun.stanford.edu/~xuepu/DATA/hccsss/ (2019).
[57] M. J. Owens and R. J. Forsyth, The heliospheric magnetic field, Living Rev. Solar Phys. **10**, 5 (2013).
[58] J. R. Jokipii and B. Thomas, Effects of drift on the transport of cosmic rays. IV—Modulation by a wavy interplanetary current sheet, Living Rev. Solar Phys. **243**, 1115 (1981).
[59] SILSO World Data Center, The International Sunspot Number (1749–2019), http://www.sidc.be/silso/.
[60] J. Becker Tjus and L. Merten, Closing in on the origin of Galactic cosmic rays using multimessenger information, Phys. Rep. **892**, 98 (2020).